

Giovanni News

Editor's Note:

Hello! This is a slightly delayed issue of *The Giovanni News* for Quarter 2 of the year 2019. The reason that is slightly delayed is that we waited for the 4th Gregory G. Leptoukh Online Giovanni Workshop to be completed, because the workshop included the announcement of the new selections for the Giovanni Image Hall of Fame, which are shown and described in this issue. In addition to that, this issue also includes citations of all of papers containing figures that were considered for the Hall of Fame (in case anyone was wondering if we noticed). While the image selections are the main feature of this issue, there is also a featured paper, a slogan (of course), and a couple of other informational items. I hope you'll find this issue interesting, informative, and perhaps even inspiring. The images show creative uses of data and graphical presentation, and that is useful to all of us in the geophysical sciences.

Jim Acker
Editor, *The Giovanni News*

Featured Research Paper:

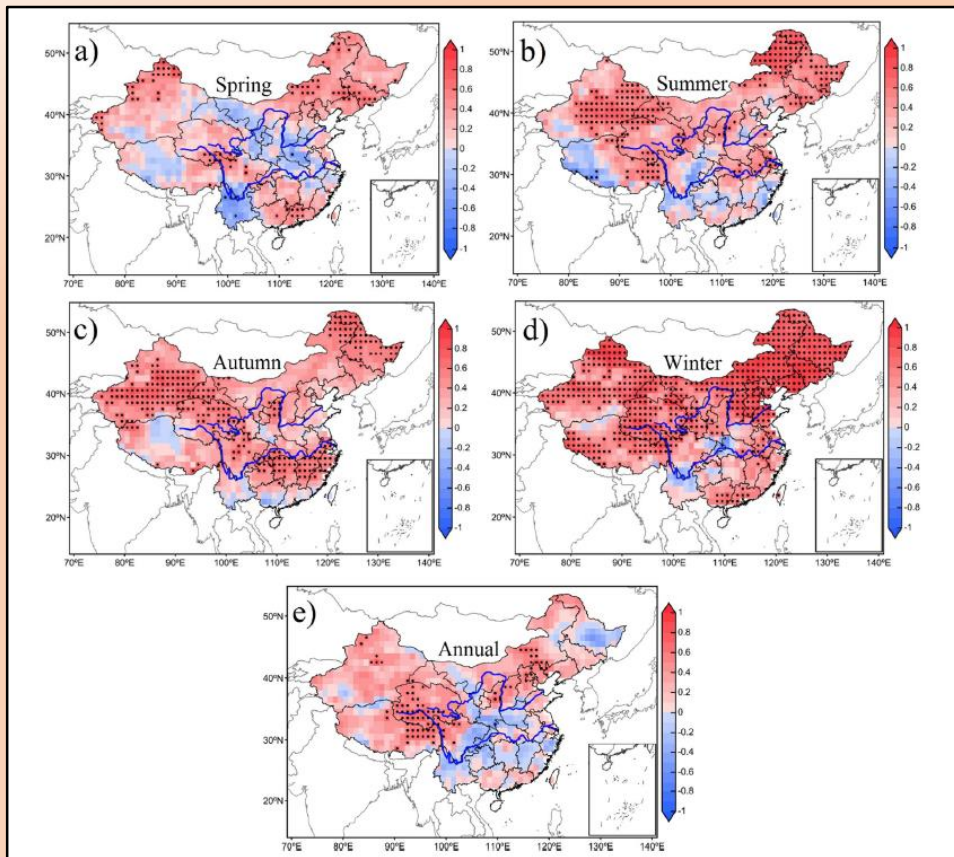
Bodenheimer, S., Lensky, I. M., and Dayan, U. (2019) Characterization of eastern Mediterranean dust storms by area of origin; North Africa vs. Arabian Peninsula. *Atmospheric Environment*, **198**, 158-165, doi:10.1016/j.atmosenv.2018.10.034.

In this paper, the authors examined the characteristics of 53 dust storms that affected the Eastern Mediterranean basin. There were distinct differences between storms originating from the Sahara Desert environs and the Arabian Peninsula. Saharan (western origin) storms lasted longer, had higher dust concentrations, and had higher wind speeds than Arabian dust storms. The higher concentrations of dust were attributed to mobilization and transport of dust occurring simultaneously for western origin storms, as compared to eastern storms where mobilization and transport were separated in time.

Data from several different sensors and ground stations in Israel were used in this study. Satellite sensors included CALIPSO* and SEVIRI*. Giovanni was used to acquire hourly MERRA-2* Aerosol Optical Thickness (AOT) data to determine the time of peak atmospheric dust concentration for each dust storm.

*CALIPSO - Cloud-Aerosol LIDAR and Infrared Pathfinder Satellite; SEVIRI - Spinning Enhanced Visible and Infrared Imager; MERRA-2 - Modern-Era Retrospective analysis for Research and Applications-2.

The Giovanni Image Hall of Fame



Modified caption:

Figure 9. Spatial distribution of correlation coefficients between annual mean MODIS Precipitable Water Vapor and surface temperature from 2001 to 2014 for (a) spring, (b) summer, (c) autumn, (d) winter, and (e) annual. The stippled areas indicate the positive and negative trends statistically significant at the 95% confidence level.

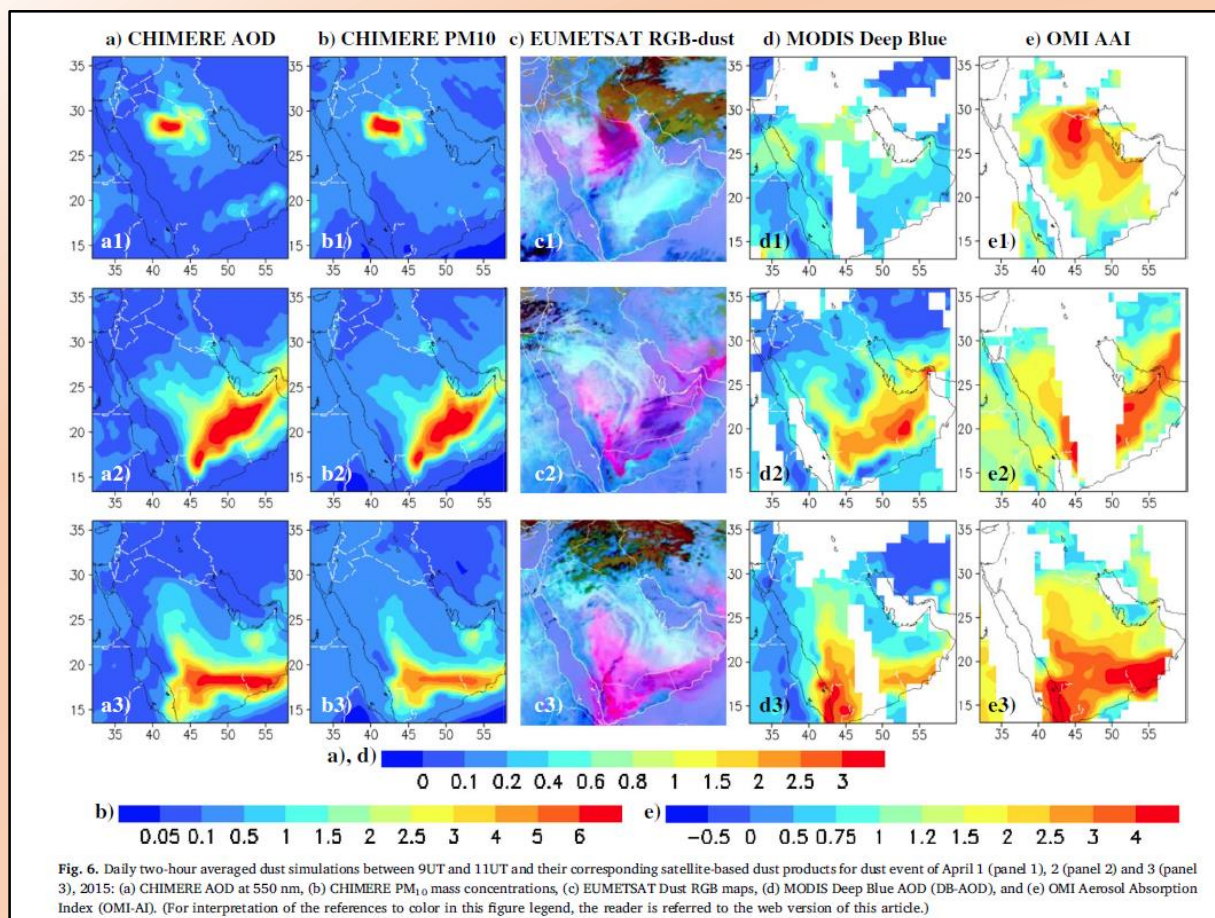
Why it was selected:

This figure uses one of Giovanni's lesser-utilized visualization capabilities, the correlation map, to show seasonal and annual correlations between precipitable water vapor and surface temperature. The figure is well-labeled, easy to comprehend, and shows changing patterns, particularly in the spring season.

Reference:

Gui, K., Che, H., Chen, Q., Zeng, Z., Zheng, Y., Long, Q., Sun, T., Liu, X., Wang, Y., Liao, T., Yu, J., Wang, H., and Zhang, X. (2017) Water vapor variation and the effect of aerosols in China. *Atmospheric Environment*, **165**, 322-335, doi:10.1016/j.atmosenv.2017.07.005.

The Giovanni Image Hall of Fame



Modified caption:

Figure 6. Daily two-hour averaged dust simulations between 9UT and 11UT and their corresponding satellite-based dust products for dust event of April 1 (panel 1), 2 (panel 2) and 3 (panel 3), 2015: (a) CHIMERE AOD at 550 nm, (b) CHIMERE PM₁₀ mass concentrations, (c) EUMETSAT Dust RGB maps, (d) MODIS Deep Blue AOD (DB-AOD), and (e) OMI Aerosol Absorption Index (OMI-AI).

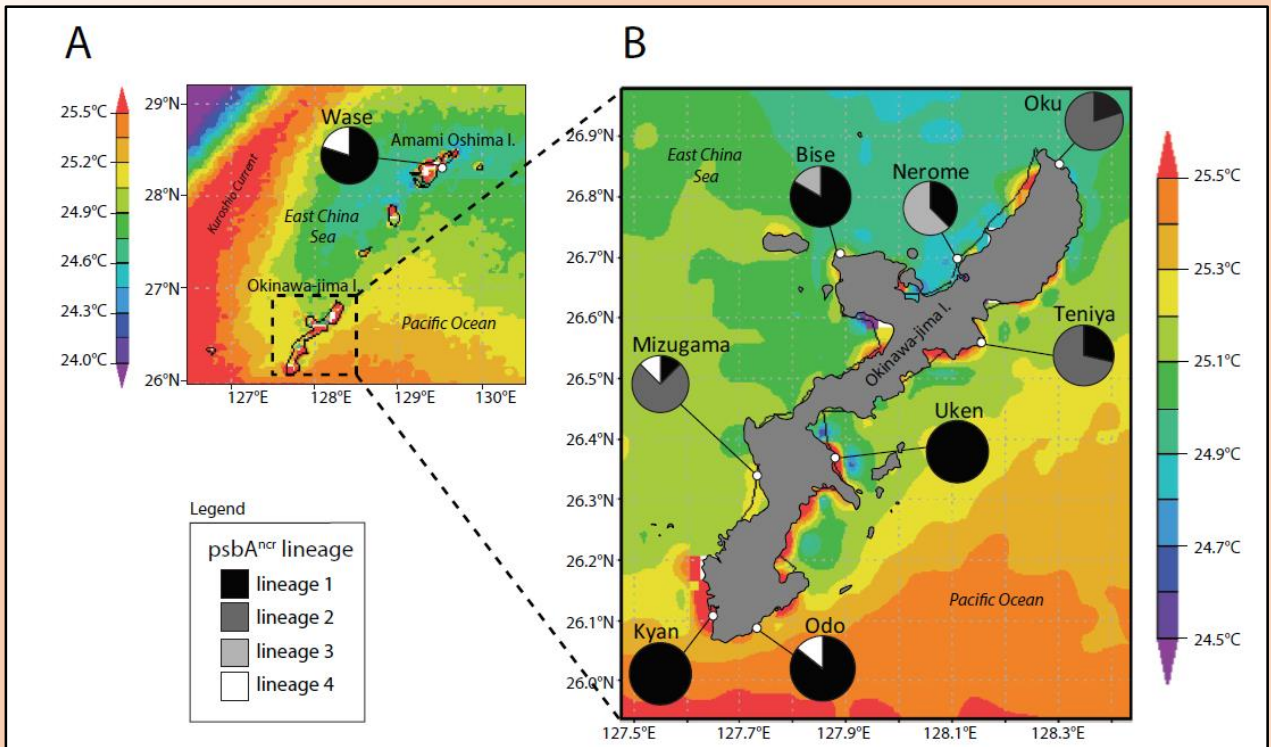
Why it was selected:

The figure shows an effective comparison of model results and observational data, using Giovanni for the observational data maps of both MODIS and OMI data. In addition to being a useful comparison, it also shows why having data from more than one satellite instrument is desirable.

Reference:

Beegum, S.N., Gherboudj, I., Chaouch, N., Temimi, M., and Ghedira, H. (2017) Simulation and analysis of synoptic scale dust storms over the Arabian Peninsula. *Atmospheric Research*, **199**, 62-81, doi:10.1016/j.atmosres.2017.09.003.

The Giovanni Image Hall of Fame



Caption:

Figure 2 Map of Amami Oshima Island (A) and Okinawa-jima Island (B) with average sea surface temperature (SST_{avg}) and *Symbiodinium* *psbA*^{ncr} lineage ratios at each site investigated. Note thermal distortions near coastlines were ignored in all SST analyses as these are generated by influence of terrestrial portions of islands within the 4 km resolution of satellite data.

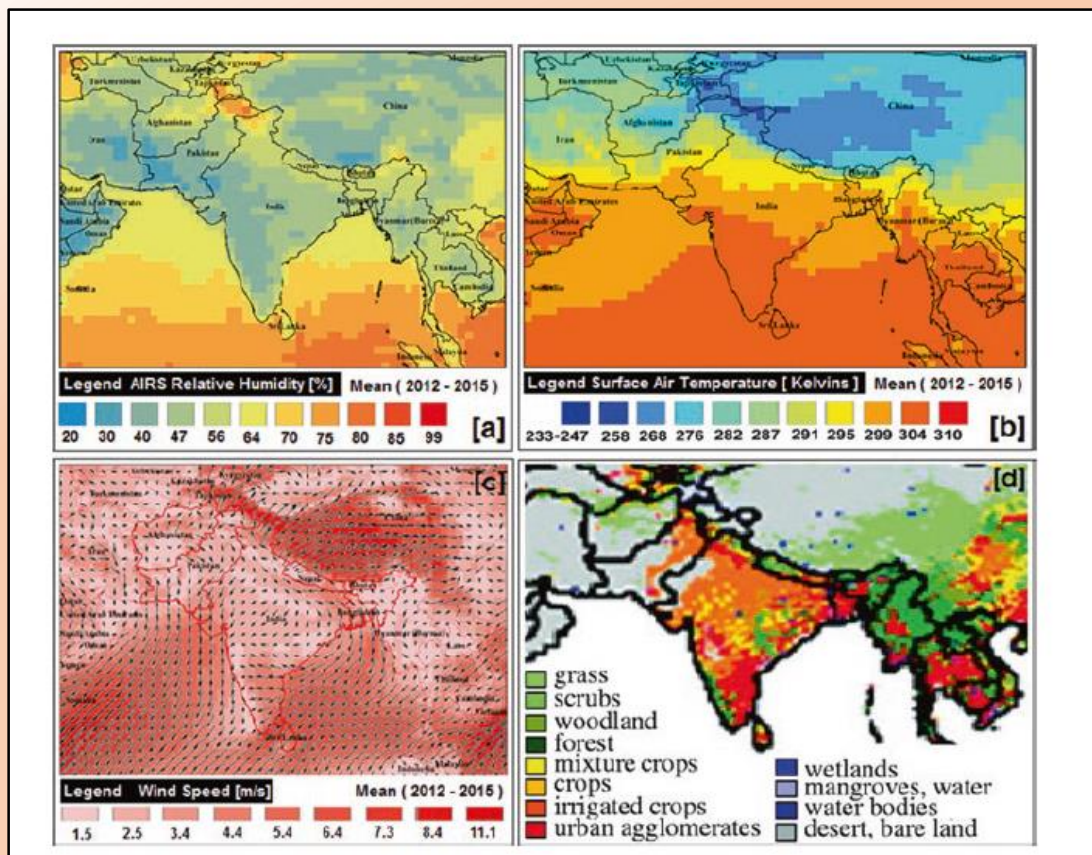
Why it was selected:

The image is colorful, using a Giovanni-generated map of sea surface temperature as the background showing the location of the different study areas and the genetic variation of the coral *endosymbionts* (also known as symbiotic algae). The genetic variation is accessible due to the way it is presented, even though the method for determining it may be unfamiliar. Furthermore, coral bleaching, the release of endosymbionts when corals are environmentally stressed, is an important concern of global change effects in the ocean.

Reference:

Noda, H., Parkinson, J.E., Yang, S.-Y., and Reimer, J.D. (2017) A preliminary survey of zoantharian endosymbionts shows high genetic variation over small geographic scales on Okinawa-jima Island, Japan. *PeerJ*, **5**:e3740; doi:10.7717/peerj.3740.

The Giovanni Image Hall of Fame



Modified caption:

Figure 22.2 shows meteorological parameters: (a) relative humidity in percent obtained from AIRS satellite instrument; (b) surface air temperature in Kelvins obtained from AIRS; (c) wind speed in m/s obtained from Modern-Era Retrospective analysis for Research and Applications (MERRA) data averaged over months of December, January, and February for all winters (2012–2015); (d) shows the land cover per grid cell for agro-ecology zones (FAO Database) obtained from their website.

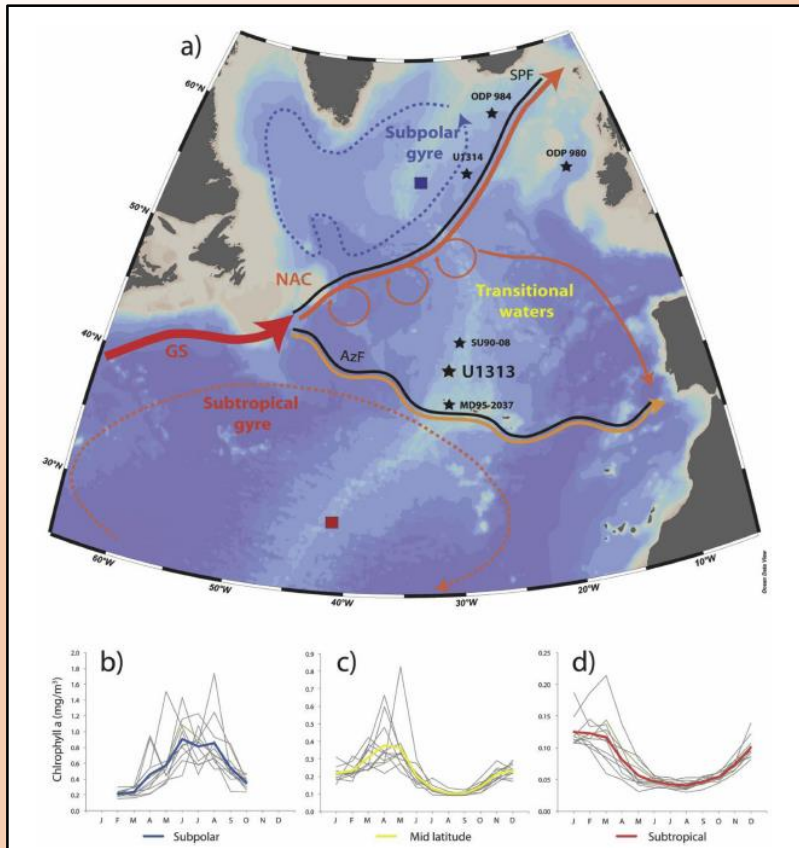
Why it was selected:

In addition to displaying three data variables obtained from Giovanni, the figure also utilizes Giovanni's seasonal averaging capability to create images for the winter (DJF) season for the years 2012-2015. The image is thus vital for the research described in this book chapter on winter aerosols in central India.

Reference:

Khokhar, M.F., and Yasmin, N. (2018) Investigating the aerosol type and spatial distribution during winter fog conditions over Indo-Gangetic plains. Chapter 22, pages 471-497 in K.P. Vadrevu, T. Ohara, and C. Justice (Eds.), *Land-Atmospheric Research Applications in South and Southeast Asia*, Springer Remote Sensing/Photogrammetry, Springer, Cham, doi:10.1007/978-3-319-67474-2_22.

The Giovanni Image Hall of Fame



Modified caption:

Figure 1. Study area: (a) Schematic surface ocean circulation of the North Atlantic, in the vicinity of IODP Site U1313. Major currents and oceanic fronts: Gulf Stream (GS, in red), North Atlantic Current (NAC, in dark orange), Azores Current (AC, in light orange); and associated fronts: Subpolar Front (SPF) and Azores Front (AzF) e both as black lines. Black stars evidence sediment data: IODP Site U1313 (this study), IODP Site U1314 (Alonso-Garcia et al., 2011), ODP Site 980 and 984 (Oppo et al., 1998 and Ortiz et al., 1999, respectively), cores SU90-08 and MD95-2037 (Villanueva et al., 2001). Map template made with Ocean Data View (Schlitzer, 2015). Note different scales of the monthly chlorophyll *a* concentration represented in (b), (c) and (d) for the different production regimes, respectively: (b) subpolar (represented by the blue square located at 55 – 57 N, 31 – 33 W), (c) for the midlatitude (black star at the location of IODP Site U1313, 40 – 42 N, 31 – 33 W) and (d) for the subtropical production regimes (red square located at 30 – 32 N, 41 – 43 W). Blue, yellow and red heavy lines indicate an average of ten years for each regime, respectively, whereas grey lines are individual years (2003–2013). Chlorophyll *a* concentration derived from MODIS and SeaWiFS satellite data available at <http://disc.sci.gsfc.nasa.gov/giovanni>.

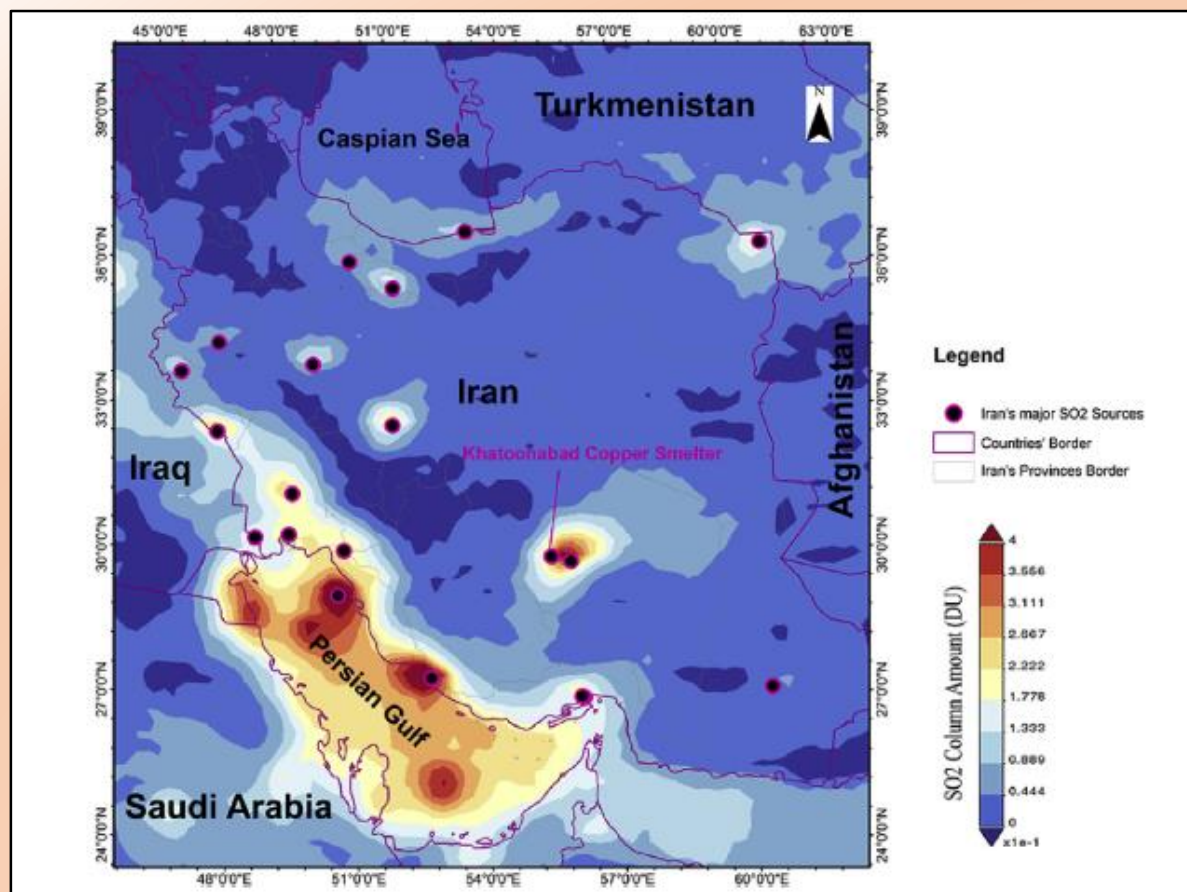
Why it was selected:

There's a lot of information here, showing the oceanic context for an analysis of drill cores. Bathymetry, major current features, and interactions are all shown. Giovanni was used to produce the three plots at the bottom, showing both yearly and a 10-year average of chlorophyll *a* concentrations for the three designated sites. Both for graphic presentation and information content, this image is outstanding.

Reference:

Cavaleiro, C., Voelker, A.H.L., Stoll, H., Baumann, K.-H., Kulhanek, D.K., Naafs, B.D.A., Stein, R., Grützner, J., Ventura, C., and Kucera, M. (2018) Insolation forcing of coccolithophore productivity in the North Atlantic during the Middle Pleistocene. *Quaternary Science Reviews*, **191**, 318–336, doi:10.1016/j.quascirev.2018.05.027.

The Giovanni Image Hall of Fame



Modified caption:

Fig. 1. Location of Iran's major SO₂ emission sources coupled with the time-averaged map of SO₂ column amount in the Planetary Boundary Layer (PBL) over 2005–2016 acquired from the Ozone Monitoring Instrument (OMI).

Why it was selected:

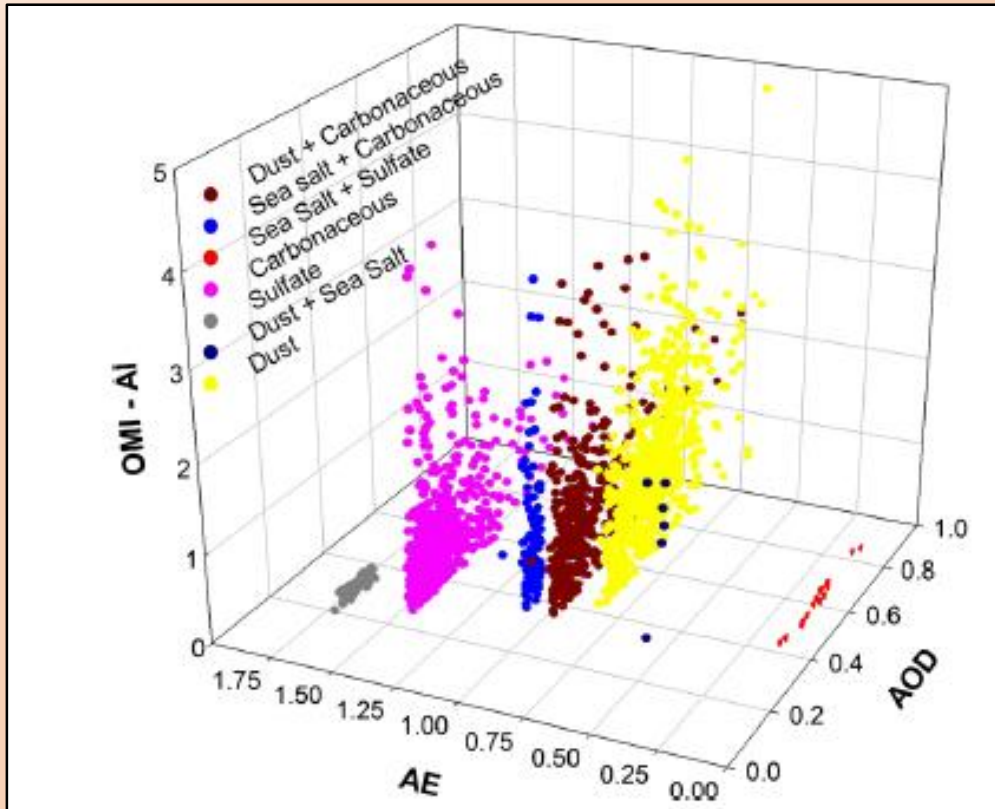
This is a very easy-to-understand depiction of the SO₂ atmospheric concentrations in the region for an 11-year period, created using Giovanni's highly useful averaging capability.

Reference:

Salmabadi, H., and Saeedi, M. (2018) Determination of the transport routes of and the areas potentially affected by SO₂ emanating from Khatoonabad Copper Smelter (KCS), Kerman province, Iran using HYSPLIT. *Atmospheric Pollution Research*, doi:10.1016/j.apr.2018.08.008.

The Giovanni Image Hall of Fame

Noted for Special Recognition



Caption:

Fig. 9 Scatter diagram between AOD, AE, and OMI-AI for determining the diverse aerosol types on an annual basis.

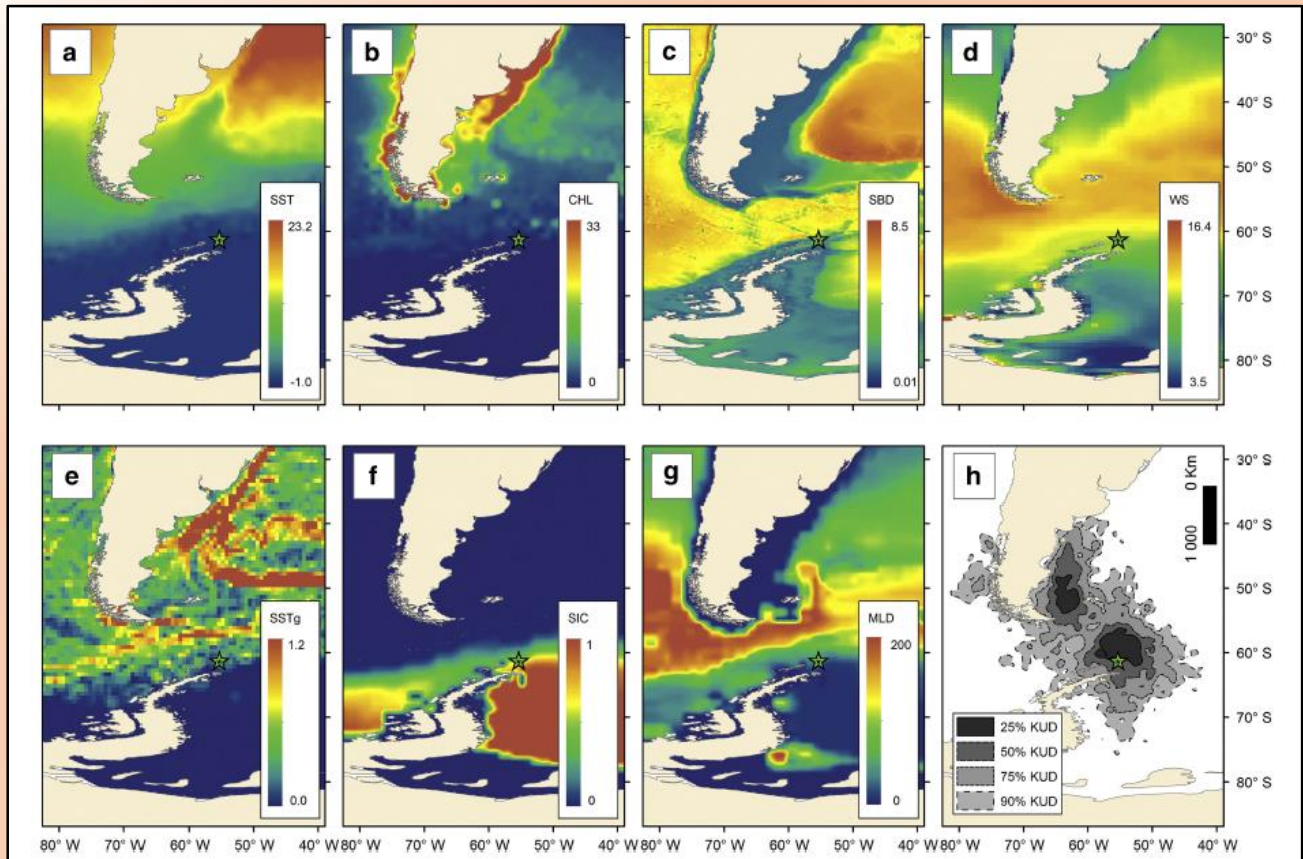
Why it was selected:

This is the first time that data acquired from Giovanni was used in a three-dimensional diagram. In addition to that novelty, the plot shows how well the data discriminate between the various aerosol types using both color and location. So this plot provides information that is easy to comprehend visually, despite the multitude of aerosol types and various combinations it depicts.

Reference:

Al-Salihi, A.M. (2018) Characterization of aerosol type based on aerosol optical properties over Baghdad, Iraq. *Arabian Journal of Geosciences*, **11**: 633, 15 pages, doi:10.1007/s12517-018-3944-1.

The Giovanni Image Hall of Fame



Caption:

Figure 1. Environmental variables used in this study. a. Sea surface temperature, SST (°C). b. Chlorophyll *a* concentration, CHL (mg m^{-3}). c. Sea bed depth, SBD (km). d. Surface wind speed, WS (m s^{-1}). e. Sea surface temperature gradient, SSTg (°C). f. Sea ice cover, SIC (proportion). g. Mixed layer depth, MLD (m). Non-breeding distribution (h) of all the tracked southern giant petrels breeding at Stinker Point, Elephant Island (star) measured as kernel usage density (KUD); for sex-level KUD see Krüger et al. (2017).

Why it was selected:

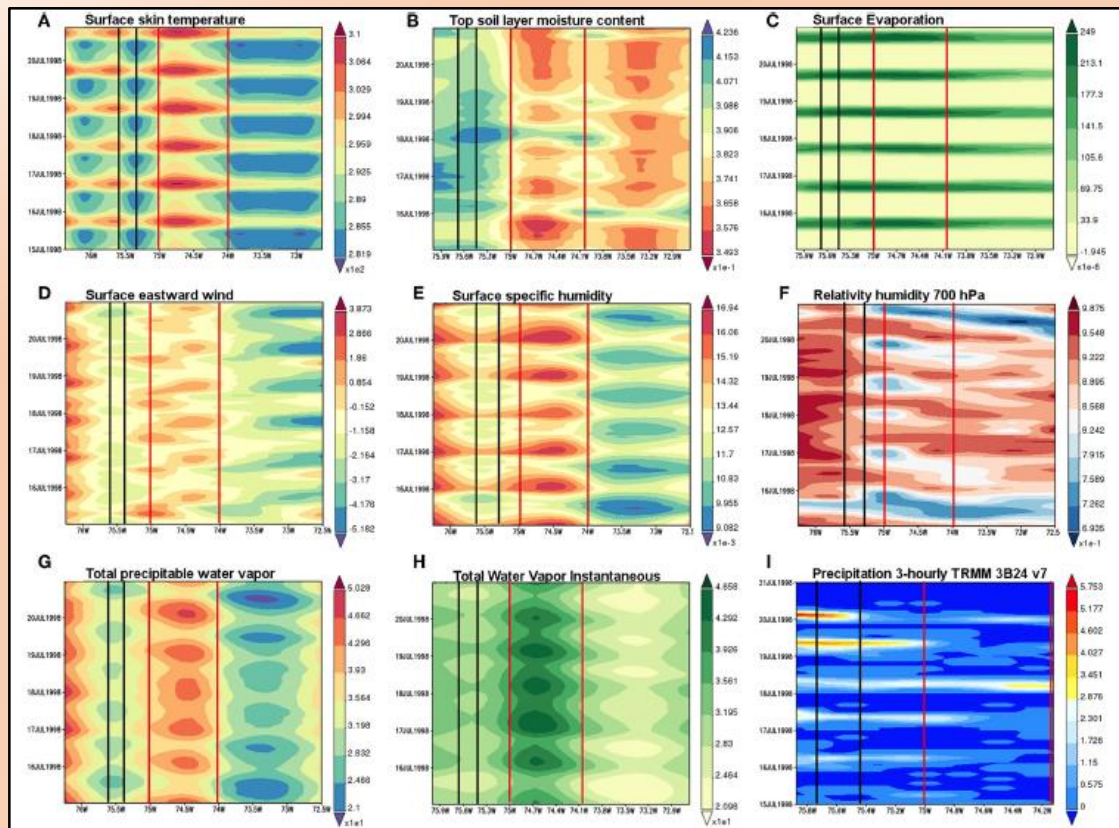
Using a combination of data variables acquired from Giovanni with other data, the authors effectively illustrate several factors that may affect the distribution of the avian species they are studying in this remote region.

Reference:

Krüger, L., Paiva, V.H., Finger, J.V.G., Petersen, E., Xavier, J., Petry, M.V., and Ramos, J.A. (2018) Intra-population variability of the non-breeding distribution of southern giant petrels *Macronectes giganteus* is mediated by individual body size. *Antarctic Science*, 7 pages, doi:10.1017/S0954102018000238.

The Giovanni Image Hall of Fame

Noted for Special Recognition



Modified caption:

Figure 7. Hovmöller time-latitude diagrams averaged over 5N to 6N for the 6-day period spanning between 15 and 21 July of 1998 with 3-h timesteps (A) Surface Skin temperature, (B) Top soil layer moisture, (C) Surface Evaporation, (D) Surface eastward wind, (E) Surface Specific Humidity, (F) Relative humidity at 700 hPa after moist (MERRA 2), (G) Total precipitable water, (H) Total water vapor, and (I) Precipitation (TRMM 3B42 v.7). The Magdalena Valley (Aburrá Valley) location is enclosed in red (black) lines.

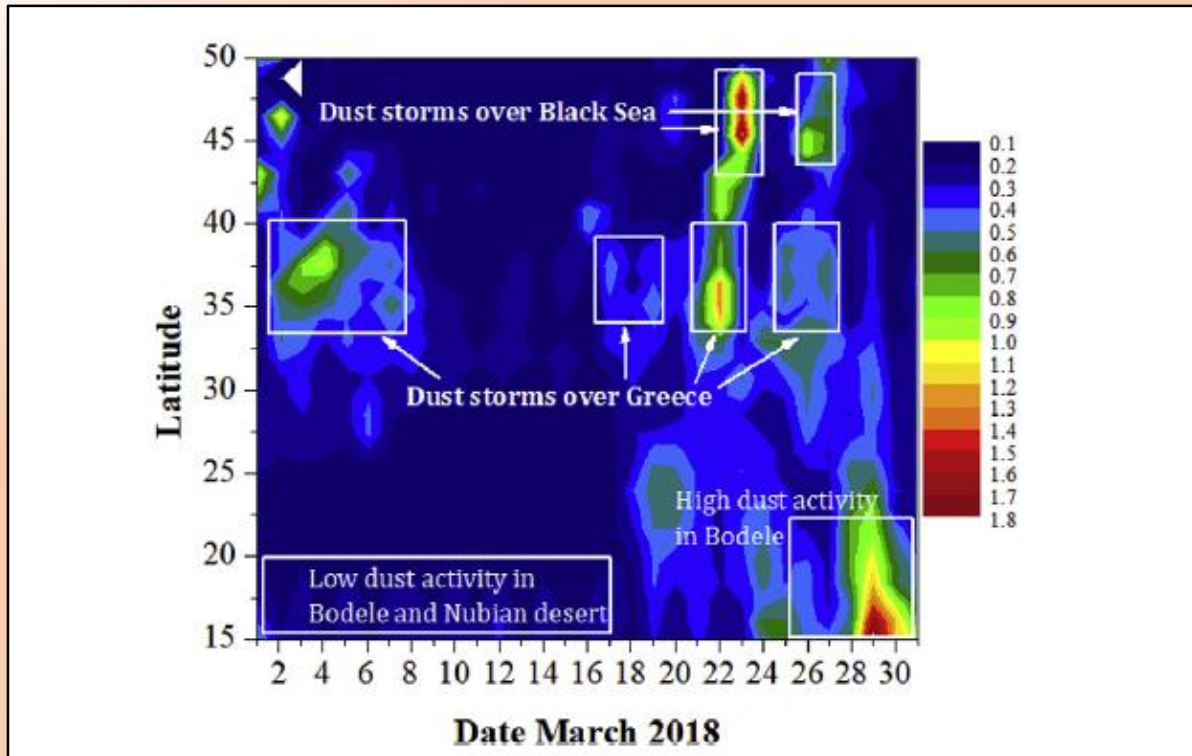
Why it was selected:

First, this image is visually striking. Second, the data show both symmetry and dichotomy in a relatively small region. Third, the plots use Giovanni's Hovmöller plot visualization option. Fourth, the plots make effective use of both MERRA-2 and precipitation data. Fifth, the authors also illustrate the valley locations on the Hovmöller plots. Finally, the plots show what the title of the paper indicates they should. This is an exemplary scientific figure.

Reference:

Bedoya-Soto, J.M., Aristizábal, E., Carmona, A.M., and Poveda, G. (2019) Seasonal shift of the diurnal cycle of rainfall over Medellín's Valley, Central Andes of Colombia (1998–2005). *Frontiers in Earth Science*, **7**:92, doi:10.3389/feart.2019.00092.

The Giovanni Image Hall of Fame



Caption:

Fig. 3. Daily variation of the longitude-averaged (15° – 35°E) Terra-MODIS AOD₅₅₀ from 15° to 50°N during March 2018.

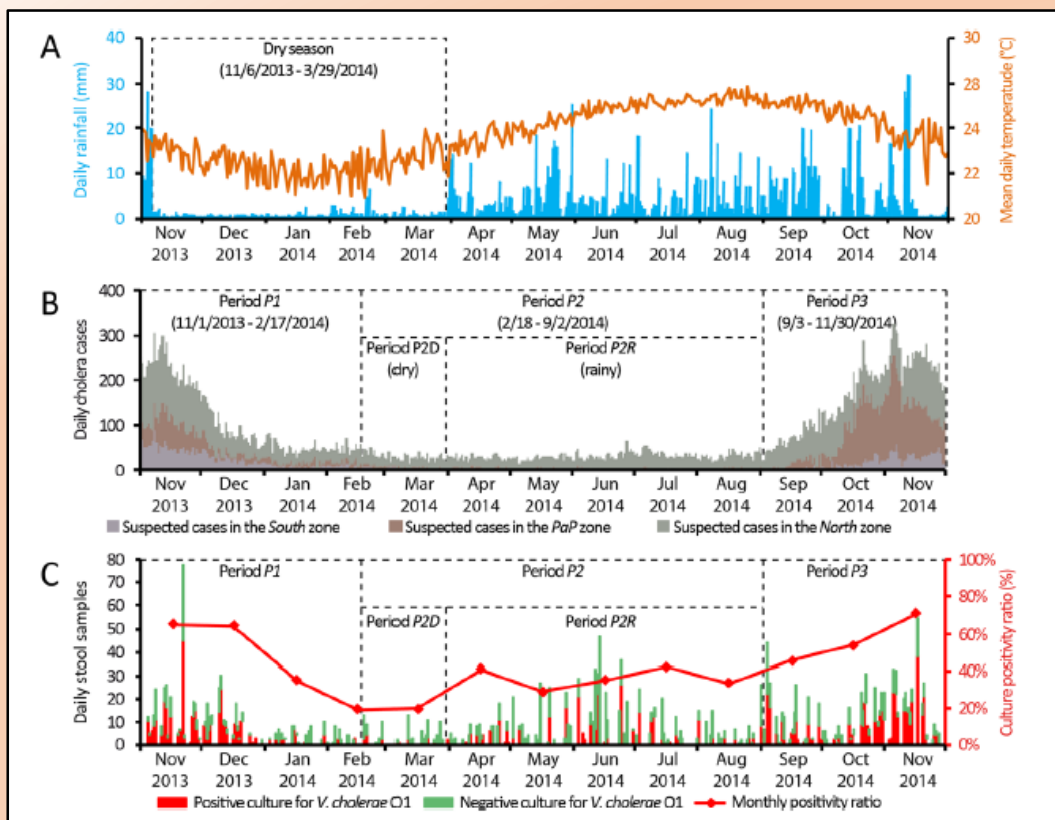
Why it was selected:

This image also uses Giovanni's Hovmöller plot visualization option, effectively showing the temporal and regional occurrence of dust storms in the region during March 2018. The image is appealing to the eye, demonstrates the various dust storm outbreak areas and affected regions, and also illustrates a fairly unique event. During this month, some of the dust from these storms made it to snow-covered peaks in Europe, causing recent snowfalls to appear tinged with orange.

Reference:

Kaskaoutis, D.G., Dumka, U.C., Rashki, A., Psiloglou, B.E., Gavriil, A., Mofidi, A., Petrinoli, K., Karagiannis, D., and Kambezidis, H.D. (2019) Analysis of intense dust storms over the eastern Mediterranean in March 2018: Impact on radiative forcing and Athens air quality. *Atmospheric Environment*, **209**, 23-39, doi:10.1016/j.atmosenv.2019.04.025.

The Giovanni Image Hall of Fame



Caption:

Figure 1. Daily evolution of cholera in Haiti between November 2013 and November 2014: (Panel A) averaged daily accumulated rainfall in Haiti and derived dry season (see S2 Appendix for details); (Panel B) daily number of suspected cholera cases in the North, PaP (Port-au-Prince) and South zones as well as derived epidemic periods identified by the temporal cluster analysis; and (Panel C) daily number of stool samples for culture confirmation of cholera and monthly culture positivity ratio. Period P1 covers the late 2013 incidence peak and the abrupt decrease in cases during the 2013–2014 dry season; Period P2 covers a lull phase that extended through the end of the dry season (P2D) and the first months of the rainy season (P2R); Period P3 represents the intense epidemic recurrence that started in September 2014.

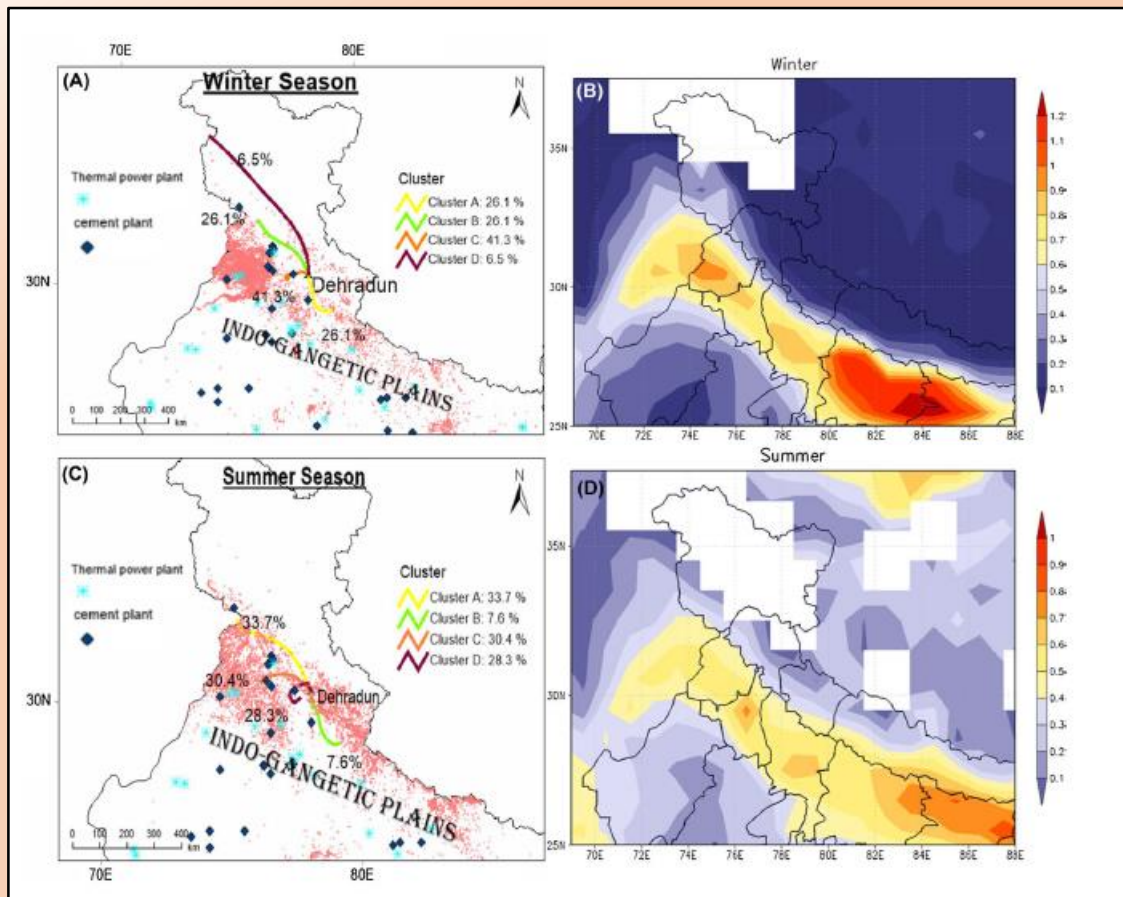
Why it was selected:

This image applies Giovanni data in an analysis of a public health concern: outbreaks of cholera in Haiti. The top panel shows a daily time-series of rainfall data, and the figure shows when Haiti's wet and dry seasons occur, and how cases of cholera are temporally related to the island country's weather.

Reference:

Rebaudet, S., Moore, S., Rossignol, E., Bogueau, H., Gaudart, J., Normand, A.-C., Laraque, M.-J., Adrien, P., Boncy, J., and Piarroux, R. (2019) Epidemiological and molecular forensics of cholera recurrence in Haiti. *Scientific Reports*, **9**, 1164, 11 pages, doi:10.1038/s41598-018-37706-0.

The Giovanni Image Hall of Fame



Caption:

Figure 4. Air mass back trajectory-clusters (a, b, c and d), MODIS derived forest spots (denoted by red dots), cement industries (denoted by diamond), and thermal power plant (denoted by cross mark) around the vicinity of the sampling site during winter and summer season is represented in the left top and bottom panel, respectively. Spatial distribution of monthly average Terra-MODIS retrieved AOD (1° × 1°) at 550 nm is represented in the right top (winter season) and bottom figures (summer season).

Why it was selected:

This image succinctly compresses a great deal of information. It shows pollution sources, transport pathways of pollutants, and seasonal changes (using Giovanni averaging) for an important public health concern related to air quality.

Reference:

Prabhu, V., Shridhar, V., and Choudhary, A. (2019) Investigation of the source, morphology, and trace elements associated with atmospheric PM₁₀ and human health risks due to inhalation of carcinogenic elements at Dehradun, an Indo-Himalayan city. *SN Applied Sciences*, **1:429**, 11 pages, doi:10.1007/s42452-019-0460-1.

The Giovanni Image Hall of Fame:

Candidate Citations

Figure 4 from: Abrams, W., Ghoneim, E., Shew, R., LaMaskin, T., Al-Bloushi, K., Hussein, S., AbuBakr, M., Al-Mulla, E., Al-Awar, M., and El-Baz, F. (2018) Delineation of groundwater potential (GWP) in the northern United Arab Emirates and Oman using geospatial technologies in conjunction with Simple Additive Weight (SAW), Analytical Hierarchy Process (AHP), and Probabilistic Frequency Ratio (PFR) techniques. *Journal of Arid Environments*, **157**, 77-96, doi:10.1016/j.jaridenv.2018.05.005.

Figure 8 from: Ahmad, T., Pandey, A.C., and Kumar, A. (2018) Flood hazard vulnerability assessment in Kashmir Valley, India using geospatial approach. *Physics and Chemistry of the Earth, Parts A/B/C*, in press, 13 pages, doi:10.1016/j.pce.2018.02.003.

Figure 4 from: Amaya, O., Quintanilla, R., Stacy, B.A., Dechraoui Bottein, M.-Y., Flewelling, L., Hardy, R., Dueñas, C., and Ruiz, G. (2018) Large-scale sea turtle mortality events in El Salvador attributed to paralytic shellfish toxin-producing algae blooms. *Frontiers in Marine Science*, 5:411, 10 pages, doi: 10.3389/fmars.2018.00411.

Figure 1 from: Bali, K., Mishra, A.K., Singh, S., Chandra, S., and Lehahn, Y. (2019) Impact of dust storm on phytoplankton bloom over the Arabian Sea: a case study during March 2012. *Environmental Science and Pollution Research*, 11 pages, doi:10.1007/s11356-019-04602-7.

Figure 8 from: Ceca, L.S.D., Ferreyra, M.F.G., Lyapustin, A., Chudnovsky, A., Otero, L., Carreras, H., and Barnaba, F. (2018) Satellite-based view of the aerosol spatial and temporal variability in the Córdoba region (Argentina) using over ten years of high-resolution data. *ISPRS Journal of Photogrammetry and Remote Sensing*, doi:10.1016/j.isprsjprs.2018.08.016.

Figure 15 from: Chang, L. T.-C., Duc, H.N., Scorgie, Y., Trieu, T., Monk, K., and Jiang, N. (2018) Performance evaluation of CCAM-CTM regional airshed modelling for the New South Wales greater metropolitan region. *Atmosphere*, **9**, 486, 31 pages, doi:10.3390/atmos9120486.

The Giovanni Image Hall of Fame:

Candidate Citations

Figure 4 from: Chen, H., Zhuang, B., Liu, J., Wang, T., Li, S., Xie, M., Li, M., Chen, P., and Zhao, M. (2019) Characteristics of ozone and particles in the near-surface atmosphere in the urban area of the Yangtze River Delta, China. *Atmospheric Chemistry and Physics*, **19**, 4153-4175, doi:10.5194/acp-19-4153-2019.

Figure 2 from: Das, D., Chakrabarty, M., Goswami, S., Basu, D., and Chaudhuri, S. (2018) Impact of intra-seasonal oscillations of Indian summer monsoon on biogeochemical constituents of North Indian Ocean. *Theoretical and Applied Climatology*, 10 pages, doi:10.1007/s00704-018-2518-1.

Figure 2 from: El-Nobi, E.F. (2018) Erythemal UV dose rate spatial distribution using Ozone Monitoring Instrument satellite data over Egypt. *European Journal of Engineering Research and Science*, **3(10)**, 21-27, doi:10.24018/ejers.2018.3.10.903.

Figure 3 from: Gómez, D., Salvador, P., Sanz, J., Casanova, C., and Casanova, J.L. (2018) Detecting areas vulnerable to sand encroachment using remote sensing and GIS techniques in Nouakchott, Mauritania. *Remote Sensing*, **10**, 1541, doi:10.3390/rs10101541, 18 pages.

Figure 6 from: Hu, K., Kumar, K.R., Kang, N., Boiyo, R., and Wu, J. (2017) Spatiotemporal characteristics of aerosols and their trends over mainland China with the recent Collection 6 MODIS and OMI satellite datasets. *Environmental Science and Pollution Research*, 19 pages, doi:10.1007/s11356-017-0715-6.

Figure 1 from: Ialongo, I., Fioletov, V., McLinden, C., Jåfs, M., Krotkov, N., Li, C., and Tamminen, J. (2018) Application of satellite-based sulfur dioxide observations to support the cleantech sector: Detecting emission reduction from copper smelters. *Environmental Technology & Innovation*, **12**, 172-179, doi:10.1016/j.eti.2018.08.006. [compare to Figure 1 of Salmabadi and Saaedi (2018)]

Figure 8 from: Janssen, T.A.J., Ametsitsi, G.K.D., Collins, M., Adu-Bredu, S., Oliveras, I., Mitchard, E.T.A., and Veenendaal, E.M. (2018) Extending the baseline of tropical dry forest loss in Ghana (1984–2015) reveals drivers of major deforestation inside a protected area. *Biological Conservation*, **218**, 163-172, doi:10.1016/j.biocon.2017.12.004.

The Giovanni Image Hall of Fame:

Candidate Citations

Figure 3b from: Jin, M.S. (2018) The relationship between surface temperatures and building electricity use: a potential new weather application. *Journal of Buildings and Sustainability*, **1(1)**, 11 pages.

Figure 2 from: Kanta, M.R., Babula, J., Anilkumar, N.P., Krishna, N.R., Bhaskar, P.V., and Melana A, S. (2017) Variability of chlorophyll-a and diatoms in the frontal ecosystem of Indian Ocean sector of the Southern Ocean. *Polish Polar Research*, **38(3)**, 375-392, doi:10.1515/popore-2017-0014.

Figure 4 from: Kaskaoutis, D.G., Rashki, A., Dumka, U.C., Mofidi, A., Kambezidis, H.D., Psiloglou, B.E., Karagiannis, D., Petrinoli, K., and Gavriil, A. (2018) Atmospheric dynamics associated with exceptionally dusty conditions over the eastern Mediterranean and Greece in March 2018. *Atmospheric Research*, **218**, 269-284, doi:10.1016/j.atmosres.2018.12.009.

Figure 6 from: Kedia, S., Kumar, R., Islam, S., Sathe, Y., and Kaginalkar, A. (2018) Radiative impact of a heavy dust storm over India and surrounding oceanic regions. *Atmospheric Environment*, **185**, 109-120, doi:10.1016/j.atmosenv.2018.05.005.

Figure 2 from: Khan, I.A., Arsalan, M.H., Siddiqui, M.F., Kiran, N., and Ajaib, M. (2016) Short-term drought assessment in Pakistan and adjoining areas by remote sensing MODIS-NDVI data: a potential consequence of climate change. *Pakistan Journal of Botany*, **48(5)**, 1887-1892.

Figure 4 from: Komurcu, M., Emanuel, K.A., Huber, M., and Acosta, R.P. (2018). High-resolution climate projections for the northeastern United States using dynamical downscaling at convection-permitting scales. *Earth and Space Science*, **5**, 26 pages, doi:10.1029/2018EA000426.

Figure 4 from: Koplitz, S.N., Mickley, L.J., Jacob, D.J., Marlier, M.E., DeFries, R.S., Gaveau, D.L.A., Locatelli, B., Reid, J.S., Xian, P., and Myers, S.S. (2018). Role of the Madden-Julian Oscillation in the transport of smoke from Sumatra to the Malay Peninsula during severe non-El Niño haze events. *Journal of Geophysical Research:Atmospheres*, **123**, 6282–6294, doi:10.1029/2018JD028533.

The Giovanni Image Hall of Fame:

Candidate Citations

Figure S3 from: Krüger, L., Pereira, J.M., Paiva, V.H., and Ramos, J.A. (2019) Personality influences foraging of a seabird under contrasting environmental conditions. *Journal of Experimental Marine Biology and Ecology*, **516**, 123-131, doi.org/10.1016/j.jembe.2019.04.003.

Figure 7 from: Kumar, A., Mishra, D.R., Equeenuddin, Sk. Md., Cho, H.J., and Rastogi, G. (2017) Differential impact of anniversary-severe cyclones on the water quality of a tropical coastal lagoon. *Estuaries and Coasts*, **40(2)**, 317-342, doi:10.1007/s12237-016-0172-3.

Figure 4 from: Kumar, A., Abouchami, W., Galer, S.J.G., Singh, S.P., Fomba, K.W., Prospero, J.M., and Andreae, M.O. (2018) Seasonal radiogenic isotopic variability of the African dust outflow to the tropical Atlantic Ocean and across to the Caribbean. *Earth and Planetary Science Letters*, **487**, 94-105, doi:10.1016/j.epsl.2018.01.025.

Figure 9 from: Kumar, K.R., Boiyo, R., Madina, A., and Kang, N. (2018) A 13-year climatological study on the variations of aerosol and cloud properties over Kazakhstan from remotely sensed satellite observations. *Journal of Atmospheric and Solar-Terrestrial Physics*, **179**, 55-68, doi:10.1016/j.jastp.2018.06.014.

Figure 12 from: Kumar, A., Bhambri, R., Tiwari, S.K., Verma, A., Gupta, A.K., and Kawishwar, P. (2019) Evolution of debris flow and moraine failure in the Gangotri Glacier region, Garhwal Himalaya: Hydro-geomorphological aspects. *Geomorphology*, **333**, 152-166, doi:10.1016/j.geomorph.2019.02.015.

Figure 2 from: Logan, T., Dong, X. and Xi, B. (2018) Aerosol properties and their impacts on surface CCN at the ARM Southern Great Plains Site during the 2011 Midlatitude Continental Convective Clouds Experiment. *Advances in Atmospheric Science*, **35**, 224-233, doi:10.1007/s00376-017-7033-2.

Figure 3 from: Lund, M.T., Myhre, G., Haslerud, A.S., Skeie, R.B., Griesfeller, J., Platt, S.M., Kumar, R., Myhre, C.L., and Schulz, M. (2018) Concentrations and radiative forcing of anthropogenic aerosols from 1750 to 2014 simulated with the Oslo CTM3 and CEDS emission inventory. *Geoscience Model Development*, **11**, 4909–4931, doi:10.5194/gmd-11-4909-2018.

The Giovanni Image Hall of Fame:

Candidate Citations

Figure 5 from: Meyer, B., Freier, U., Grimm, V., Groeneveld, J., Hunt, B.P.V., Kerwath, S., King, R., Klaas, C., Pakhomov, E., Meiners, K.M., Melbourne-Thomas, J., Murphy, E.J., Thorpe, S.E., Stammerjohn, S., Wolf-Gladrow, D., Auerswald, L., Götz, A., Halbach, L., Jarman, S., Kawaguchi, S., Krumpen, T., Nehrke, G., Ricker, R., Sumner, M., Teschke, M., Trebilco, R., and Yilmaz, N.I. (2017) The winter pack-ice zone provides a sheltered but food-poor habitat for larval Antarctic krill. *Nature Ecology and Evolution*, **1**(12), 1853-1861, doi:10.1038/s41559-017-0368-3.

Figure 1 and **Figure 3** from: Moran-Zuloaga, D., Ditas, F., Walter, D., Saturno, J., Brito, J., Carbone, S., Chi, X., Hrabě de Angelis, I., Baars, H., Godoi, R.H.M., Heese, B., N., Holanda, B.A., Lavrič, J.V., Martin, S.T., Ming, J., Pöhlker, M.L., Ruckteschler, N., Su, H., Wang, Y., Wang, Q., Wang, Z., Weber, B., Wolff, S., Artaxo, P., Pöschl, U., Andreae, M.O., and Pöhlker, C. (2017) Long-term study on coarse mode aerosols in the Amazon rain forest with the frequent intrusion of Saharan dust plumes. *Atmospheric Chemistry and Physics*, **18**, 10055–10088, doi:10.5194/acp-18-10055-2018.

Figure 4 from: Mossad, A., and Alazba, A.A. (2018) Determination and prediction of standardized precipitation index (SPI) using TRMM data in arid ecosystems. *Arabian Journal of Geosciences*, **11**, 16 pages, doi:10.1007/s12517-018-3487-5.

Figure 4 from: Pinker, R.T., Zhang, B., Weller, R. A., and Chen, W. (2018). Evaluating surface radiation fluxes observed from satellites in the southeastern Pacific Ocean. *Geophysical Research Letters*, **45**, 2404–2412. doi:10.1002/2017GL076805

Figure 8 from: Rizza, U., Miglietta, M.M., Mangi, C., Ielpoa, P., Morichetti, M., Iachini, C., Virgil, S., and Passerini, G. (2017) Sensitivity of WRF-Chem model to land surface schemes: Assessment in a severe dust outbreak episode in the Central Mediterranean (Apulia Region). *Atmospheric Research*, **201**, 168–180, doi:10.1016/j.atmosres.2017.10.022.

Figure 9 from: Rupakheti, D., Adhikary, B., Praveen, P.S., Rupakheti, M., Kang, S., Mahata, K.S., Naja, M., Zhang, Q., Panday, A.K., and Lawrence, M.G. (2017) Pre-monsoon air quality over Lumbini, a world heritage site along the Himalayan foothills. *Atmospheric Chemistry and Physics*, **17**, 11041-11063, doi:/10.5194/acp-17-11041-2017.

The Giovanni Image Hall of Fame:

Candidate Citations

Figure 2 from: Saad, M., Masmoudi, M., Chevaillier, S., Laurent, B., Lafon, S., and Alfaro, S.C. (2018) Variability of the elemental composition of airborne mineral dust along the coast of Central Tunisia. *Atmospheric Research*, **209**, 170-178, doi:10.1016/j.atmosres.2018.04.001

Figure 10.4 from: Saikawa, E., Panday, A., Kang, S., Gautam, R., Zusman, E., Cong, Z., Somanathan, E., and Adhikary, B. (2019) "Air pollution in the Hindu Kush Himalaya". Chapter 10 in: Wester, P., Mishra, A., Mukherji, A., and Shrestha, A. (Eds) *The Hindu Kush Himalaya Assessment*. Springer, Cham, doi:10.1007/978-3-319-92288-1.

Figure 4 from: Senghor, H., Machu, E., Hourdin, F., and Gaye, A.T. (2017) Seasonal cycle of desert aerosols in western Africa: analysis of the coastal transition with passive and active sensors. *Atmospheric Chemistry and Physics*, **17**, 8395-8410, doi:10.5194/acp-17-8395-2017.

Figure 4 from: Shikwambana, L., and Sivakumar, V. (2018) Investigation of various aerosols over different locations in South Africa using satellite, model simulation and LIDAR. *Meteorological Applications*, **26(2)**, 275-287, doi:10.1002/met.1761.

Figure 24.7 and **Figure 24.8** from: Tariq, S., and Ul-Haq, Z. (2018) "Satellite remote sensing of aerosols and gaseous pollution over Pakistan". Chapter 24, pages 523-549 in K.P. Vadrevu, T. Ohara, and C. Justice (Eds.) *Land-Atmospheric Research Applications in South and Southeast Asia*, Springer Remote Sensing/Photogrammetry, Springer, Cham, doi:10.1007/978-3-319-67474-2_24.

Figure 2 from: Torres, A.I., Paparazzo, F.E., Williams, G.N., Rivas, A.L., Solís, M.E., and Esteves, J.L. (2019) Dynamics of macronutrients in the San Jorge Gulf during spring and summer. *Oceanography*, **31(4)**, Special Issue On The Gulf of San Jorge (Patagonia, Argentina), 25-32.

The Giovanni Image Hall of Fame: Candidate Citations

Figure 4 from: Tutsak, E., and Koçak, M. (2019) Long-term measurements of aerosol optical and physical properties over the Eastern Mediterranean: Hygroscopic nature and source regions. *Atmospheric Environment*, **207**, 1-15, doi:10.1016/j.atmosenv.2019.03.007.

Figure 4 from: Varghese, M., Prabha, T.V., Murugavel, P., Anu, A.S., Resmi, E.A., Dinesh, G., Rao, Y.J., Nagare, B., Safai, P.D., Nair, S., Nandakumar, K., Vishnu, R., and Kumar, Y.B. (2019) Aerosol and cloud droplet characteristics over Ganges Valley during break phase of monsoon: A case study. *Atmospheric Research*, **220**, 125-140, doi:10.1016/j.atmosres.2019.01.013.

Figure 13 from: Vlasenko, V., Stashchuk, N., & Nimmo-Smith, W. A. M. (2018). Three-dimensional dynamics of baroclinic tides over a seamount. *Journal of Geophysical Research: Oceans*, 23 pages, doi:10.1002/2017JC013287.

Giovanni:
Providing **Eureka!** Moments for
Earth Science 
since 2003

<https://giovanni.gsfc.nasa.gov>

For Your Information:

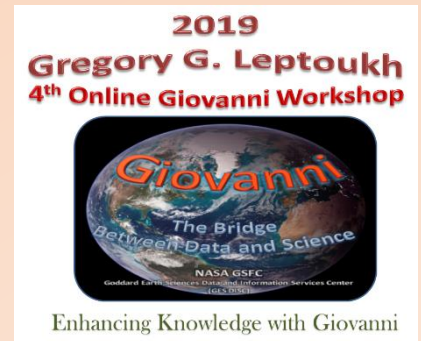
- A page about Giovanni was recently added to the U.S. Climate Resilience Toolkit. URL:

<https://toolkit.climate.gov/tool/giovanni—geospatial-interactive-online-visualization-and-analysis-infrastructure>



- All of the Webinars presented in the 4th Gregory G. Leptoukh Online Giovanni Workshop can be found at one location, courtesy of the meeting host, NASA Earthdata (<https://earthdata.nasa.gov>):

<https://www.youtube.com/watch?v=ecvGy-9B4RU&list=PLO2yB4LGNIWqhse1tan5UTLFQitLLZXYN>



- A presentation on the subject of how Giovanni can enhance the knowledge of citizen scientists was recently given by James Acker at the "Building the NASA Citizen Science Community" workshop in Tucson, Arizona. The presentation can be downloaded from this agenda page (look for presenter's name):

<https://meeting.psi.edu/citizen-science-conference-agenda-and-schedule/>

